Enabling Low-Power, Multi-Modal Neural Interfaces Through a Common, Low-Bandwidth Feature Space

Zachary T. Irwin, *Student Member, IEEE*, David E. Thompson, *Member, IEEE*, Karen E. Schroeder, Derek M. Tat, Ali Hassani, Autumn J. Bullard, Shoshana L. Woo, Melanie G. Urbanchek, *Member, IEEE*, Adam J. Sachs, Paul S. Cederna, William C. Stacey, Parag G. Patil, and Cynthia A. Chestek, *Member, IEEE*

***Abstract*—Brain-Machine Interfaces (BMIs) have shown great potential for generating prosthetic control signals. Translating BMIs into the clinic requires fully implantable, wireless systems; however, current solutions have high power requirements which limit their usability. Lowering this power consumption typically limits the system to a single neural modality, or signal type, and thus to a relatively small clinical market. Here, we address both of these issues by investigating the use of signal power in a single narrow frequency band as a decoding feature for extracting information from electrocorticographic (ECoG), electromyographic (EMG), and intracortical neural data. We have designed and tested the Multi-modal Implantable Neural Interface (MINI), a wireless recording system which extracts and transmits signal power in a single, configurable frequency band. In prerecorded datasets, we used the MINI to explore low frequency signal features and any resulting tradeoff between power savings and decoding performance losses. When processing intracortical data, the MINI achieved a power consumption 89.7% less than a more typical system designed to extract action potential waveforms. When processing ECoG and EMG data, the MINI achieved similar power reductions of 62.7% and 78.8%. At the same time, using the single signal feature extracted by the MINI, we were able to decode all three modalities with less than a 9% drop in accuracy relative to using high-bandwidth, modality-specific signal features. We believe this system architecture can be used to produce a viable, cost-effective, clinical BMI.**

***Index Terms*—Brain-machine interface (BMI), implantable, low power, multi-modal, neural interface.**

Manuscript received December 09, 2014; revised July 31, 2015; accepted October 15, 2015. Date of publication November 20, 2015; date of current version May 06, 2016. This work was supported in part by the Wallace H. Coulter Foundation, the Plastic Surgery Foundation, the Frederick A. Coller Surgical Society, and the A. Alfred Taubman Medical Research Institute. Z. T. Irwin and D. E. Thompson contributed equally to this work.

Z. T. Irwin, K. E. Schroeder, D. M. Tat, A. Hassani, A. J. Bullard, and C. A. Chestek are with the Biomedical Engineering Department, University of Michigan, Ann Arbor, MI 48109 USA (e-mail: irwinz@umich.edu; cchestek@umich.edu).

D. E. Thompson is with the Electrical and Computer Engineering Department, Kansas State University, Manhattan, KS 66506 USA.

S. L. Woo and M. G. Urbanchek are with the Plastic Surgery Section, Department of Surgery, University of Michigan, Ann Arbor, MI 48109 USA.

A. J. Sachs is with the Neurosurgery Division, Department of Surgery, University of Ottawa, Ottawa, ON K1N 6N5, Canada.

P. S. Cederna is with the Biomedical Engineering Department and the Plastic Surgery Section, Department of Surgery, University of Michigan, Ann Arbor, MI 48109 USA.

W. C. Stacey is with the Biomedical Engineering Department and the Department of Neurology, University of Michigan, Ann Arbor, MI 48109 USA.

P. G. Patil is with the Departments of Neurosurgery, Neurology, Anesthesiology, and Biomedical Engineering, University of Michigan, Ann Arbor, MI 48109 USA.

Color versions of one or more of the figures in this paper are available online at http://ieeexplore.ieee.org.

Digital Object Identifier 10.1109/TNSRE.2015.2501752

I. Introduction

BRAIN-MACHINE interfaces (BMIs) have shown great promise for generating prosthetic control signals in both monkeys [1]–[3] and humans [4], [5]. By decoding neural activity into intended movement, they offer potentially more accurate and natural control than conventional body-powered or surface-myoelectric prostheses. BMIs also have the potential to restore function in cervical-level spinal cord injury, where conventional prostheses are not applicable. However, current BMIs require a percutaneous connection from indwelling electrodes to recording devices outside the body. This introduces several major problems, including potential infection risk and limited user mobility.

To address these problems and move closer to a viable clinical BMI, many groups have designed and built wireless and implantable neural recording systems (e.g., [6]–[9]). However, none of these systems have thus far been tested in humans or approved by the FDA for clinical use. One major challenge to translating research BMIs into the clinic is the high-bandwidth nature of typical systems, which grant access to the individual neural waveforms. The need to acquire, process, and wirelessly transmit data at rates up to and well beyond 24 Mb/s [10], [11] both increases the power requirements of the device and restricts the use of wireless bands like the medical-reserved MedRadio service (which currently limits bandwidth to 6 MHz [12]).

The high power consumption of current systems results in unacceptably low battery life, unlike other implanted technologies, such as pacemakers, which can operate for years on a single battery [13]. Borton *et al.*, for example, developed a fully implantable 100-channel system which transmits broadband data at 24 Mb/s and requires 90.6 mW. This device must be recharged every 7 h when using a medical-grade 200 mAh battery [10]. Miranda *et al.* similarly built a system which consists primarily of off-the-shelf components and is capable of transmitting 32 channels of broadband data at 24 Mb/s for 143 mW [14]. Their system lasts for 33 h [14], but requires two 1200 mAh batteries which may be impractical for an implanted device.

One common method of saving power is to reduce the system bandwidth by focusing on only the BMI-relevant features of the input signal, which is typically specific to a particular neural signal type, or modality. For example, electrocorticography-based (ECoG) BMIs commonly use average signal power in particular frequency bands in order to classify intended movement [15], [16]. Zhang *et al.* designed a neural processing IC which

uses this ECoG-specific feature space by extracting and transmitting only the signal power in four separate low-frequency bands, instead of the full broadband signal [17]. This type of data compression, along with lowering the front-end bandwidth, resulted in a power consumption of only 6.4 μW for a single-channel system [17].

Commercial electromyography-based (EMG) BMIs use a similar signal feature by thresholding average waveform amplitude for on/off binary decodes [18]. Hart *et al.* reported a system containing on-board circuitry to integrate the rectified EMG, allowing for a lower sampling rate and thus reducing the data rate for processing and transmission [19]. In research-oriented EMG BMIs, pattern recognition algorithms examine waveform temporal features, requiring high sampling rates [18], [20]. However, even these types of BMIs can save power by limiting the analog pass-band to below 1 kHz [21], [22].

Intracortical BMIs typically analyze action potential ("spike") timing. Spikes are detected in the broadband signal and are binned at regular intervals to produce spike counts. These spike counts can then be used by various decoding algorithms to predict continuous movement [23], [24] or classify intended movement targets [25]. This presents an opportunity for massive data compression, as a system need only transmit spike times instead of the full $\sim$30 ks/s waveform, reducing the required data rate by $>$90% [26]–[28]. Chestek *et al.* [29] built and tested *in vivo* a system based on the 100-channel Integrated Neural Interface chip, designed by Harrison *et al.* [30], which contains integrated comparators for on-board spike detection and consumes a total of 8 mW [30]. Cheney *et al.* further limited the outgoing data rate by transmitting spike counts, instead of single detections, at 100 ms intervals [31].

Each of these systems is designed around a modality-specific signal feature, limiting the clinical use of the system to a fairly small market. A cost-effective solution might require a single, multi-modal system which could be applicable to all clinical areas. This paper describes a path to clinical viability by exploring a low-bandwidth feature space common to ECoG, EMG, and intracortical BMIs, which would allow for both low-power and multi-modal implantable systems. ECoG and EMG BMIs are both capable of using band power as the primary decoding feature, but few groups have investigated band power as an alternative to intracortical spikes. Stark and Abeles found that most, if not all, of the decoding power of spikes could also be extracted from the signal power in a band from .3–6 kHz [32]. This implies that all three neural modalities can be decoded using individual, low-bandwidth frequency bands. However, there was no discussion in that study of whether the same intracortical information could be found in a narrower band. Also, assessment of the actual power savings of such an approach, and any potential tradeoff in BMI performance, requires a physical device. Dorman *et al.* designed an intracortical recording device around this feature, using a 1 kHz low-pass filter to pass spike timing information [33], though to our knowledge the device output was never used for decoding.

We have designed and built a low-power, multi-modal neural recording system which extracts the signal power in a single, configurable frequency band and wirelessly transmits that power at regular, BMI-relevant time intervals. We validated the system using novel datasets consisting of EMG and intracortical spikes from rhesus macaques and ECoG recordings from human subjects. We explored the ability of this low-bandwidth feature space to accurately decode all three modalities and compared the power requirements of the system to that of more typical high-bandwidth systems.

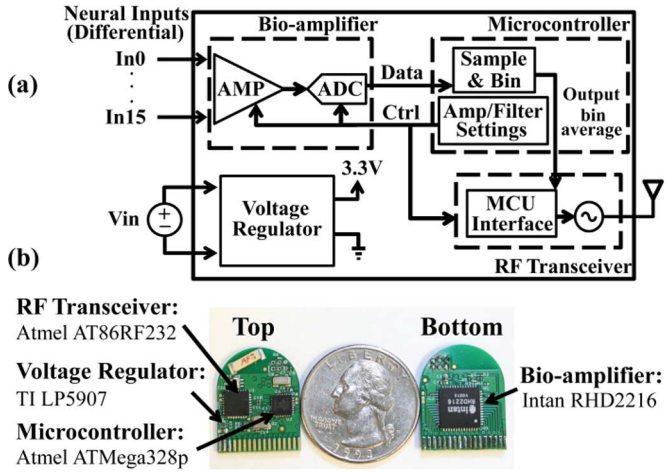

Fig. 1. (a) Block diagram of the MINI. Average signal power on each channel is computed and wirelessly transmitted at regular intervals. (b) Assembled device with labeled components.

TABLE I
MINI SYSTEM SPECIFICATIONS

Parameter	Value
# channels	16 *
ADC resolution	16 bits
Amplifier input-referred noise	2.4 μV_{RMS}
MCU clock	8 MHz
Low-pass filter	0.1 – 20 kHz *
High-pass filter	0.1 – 500 Hz *
Sampling rate	< 5 ksps (16 channels), < 40 ksps (1 channel)*
Wireless data rate	< 250 kbps *
Wireless packet rate	< 500 packets/s (16 channels), < 7500 packets/s (1 channel)
Supply voltage	3.3 V
Typical power consumption	7.5 mW **

* Configurable in software
** Parameter settings: low pass filter – 100 Hz, high pass filter – 500 Hz, sampling rate – 2 ksps, wireless data rate – 4 kbps

II. METHODS

In order to fully explore this feature space, we designed and built the Multi-modal Implantable Neural Interface (MINI), shown in Fig. 1 along with a block diagram of the system. The MINI is designed to extract and transmit the average signal power on each channel at regular time intervals and can be easily reconfigured for a wide range of analog pass-bands, sampling rates, and wireless data rates, summarized in Table I.

A. System Design

The MINI consists entirely of commercial, off-the-shelf components. The front-end is an Intan RHD2216, a 16-channel bio-amplifier and 16-bit ADC. The amplifier settings and number

of active channels can be easily configured by the central microcontroller (MCU) via a standard SPI bus to match the desired signal modality. The lower cutoff frequency of the amplifier bank is selectable from 0.1–500 Hz, while the upper cutoff range is 0.1–20 kHz. The ADC sampling rate is determined by the MCU, up to a maximum of 5 ks/s when using all 16 channels, or 40 ks/s for a single channel. The power consumption of the Intan chip scales linearly with the configured filter upper cutoff frequency and the total sampling rate, permitting an analysis of the tradeoff between signal fidelity and MINI power.

The Intan chip also internally computes the absolute value of each channel, which can be used as a simple measure of signal power. During initial decode tests in MATLAB, signal absolute value performed at least as well as more computationally complex algorithms such as mean squared value and root mean squared value for all modalities. The Intan absolute value function was thus used to save costly MCU computational time.

The wireless transceiver is an Atmel AT86RF232, which is compliant with the IEEE 802.15.4 wireless standard and has a maximum data rate of 250 kb/s at 2.4 GHz. With 16 channels and 16-bit ADC resolution, signal power can be binned and transmitted off-device roughly every 2 ms, though in typical use the transmission rate is set to $\sim$50 ms. Data and configuration settings are exchanged with the MCU through a second SPI bus.

An 8-bit Atmel ATMega328p MCU serves as the central controller and data processor, configuring the front-end and wireless, as well as controlling the dataflow from sampling to transmission. The MCU is clocked via an internal RC oscillator at 8 MHz, with a 32.768 kHz external crystal oscillator operating asynchronously from the main clock for sampling timing. The MCU itself is programmed from an external computer via a six-pin in-system interface, and system configuration settings can be easily modified in the application code. Prior to clinical translation, this physical interface could be modified to accept programming via the wireless link.

In typical use, the system is first configured for the desired modality by setting a few simple C macros in the MCU application code: changing the analog pass-band, ADC sampling rate, number of recorded channels, and wireless transmission rate. During operation, the MCU samples and buffers the absolute value of each channel. At the end of each bin period, it computes the average for each channel and passes the data to the wireless transceiver for transmission off-device. Outside the system, a remote recording system receives the data sent at each bin period, which can be stored or input into a decoding algorithm for prosthetic control.

B. Study Design and Device Validation

We used the MINI to explore the relationship between power consumption and decoding performance, analyzing four datasets containing neural and hand kinematic data recorded during similar finger movement tasks. ECoG data were obtained from two human subjects undergoing invasive seizure-focus mapping, and EMG and intracortical data were obtained from two rhesus macaques performing a separate task. All neural data were recorded using a Cerebus/Neuroport amplifier (Blackrock Microsystems) with a similar noise floor to the MINI. Human and monkey protocols were approved by the University of Michigan Institutional Review Board and the University Committee on Use and Care of Animals.

For each modality, we first performed a high-bandwidth decode in MATLAB (Mathworks) using a typical feature set specific to that modality and estimated the power required to transmit and extract that feature set. We then, also in MATLAB and using different days' datasets, searched the low-bandwidth feature space to determine the optimal frequency band and sampling rate for decoding each modality. Using that optimal configuration, we replayed the first set of neural data through the MINI, measured the power consumption, and performed a low-bandwidth decode using the output. Finally, we compared both the decode performance and the power difference between high-bandwidth and low-bandwidth approaches within each modality.

1) Behavioral Tasks: A human subject (P1) undergoing invasive ECoG seizure-focus mapping performed an isometric hand movement task as described in [16]. Briefly, in several consecutive trials, the subject was asked to perform and hold a fist grasp, pinch grasp, or flexion of an individual finger for four seconds, before returning to a neutral hand position for an additional four seconds. Hand kinematics were recorded via a DataGlove 5 Ultra (5DT) containing flex sensors on each of the fingers. A real-time computer running xPC Target (Mathworks) coordinated the trial flow and synchronized the behavioral and neural data for offline analysis. A second human subject (P2) performed a passive sensory task, in which one fingertip per trial (thumb, index, or little) was brushed (in one experiment) or pressed (in a second experiment) by the experimenter for four seconds per trial.

Two monkeys performed a continuous finger movement task, illustrated in Fig. 2. Each monkey's index finger was instrumented with a flex sensor (Spectra Symbol), which fed finger position data to a real-time computer also running xPC Target. A virtual model of a monkey hand was displayed on a monitor in front of the monkey and mirrored the movements measured by the flex sensor. At the start of a trial, the xPC cued a spherical target to appear in the path of the virtual finger, and the monkey was required to flex or extend his finger to hit the target on the screen. After holding the target for $\sim$ 100 ms, the monkey was given a juice reward. Two targets, respectively requiring full flexion and full extension, were presented to the monkey in alternating trials.

2) Electrophysiology: The two human subjects were implanted with clinical subdural ECoG macroelectrode grids (Ad-Tech Medical) for seizure-focus mapping. Broadband neural data were recorded during task performance at 30 ks/s using a Neuroport signal processor (Blackrock Microsystems). Prior to analysis, the neural data were decimated to 10 ks/s, and each channel was rereferenced to the common average of its corresponding 32-channel cable into the amplifier [34]. Rereferencing was necessary to remove the noise introduced on the $\sim$3 ft recording cables by the hospital room environment.

Finger flexion-related EMG was recorded from one monkey during task performance via a pair of percutaneous fine-wire electrodes. The differential signal from these electrodes was filtered by a DAM50 amplifier (WPI) between 10–1000 Hz before

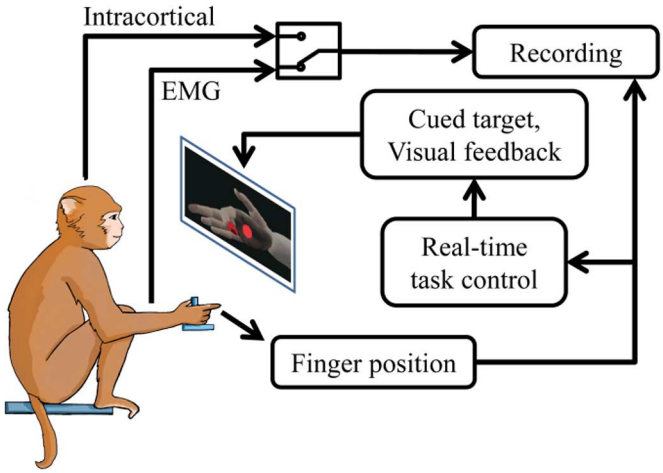

Fig. 2. Monkey finger movement task. The monkey was required to hit virtual targets by flexing or extending his fingers. Hand movements were measured via flex sensors and recorded along with either intracortical or EMG data.

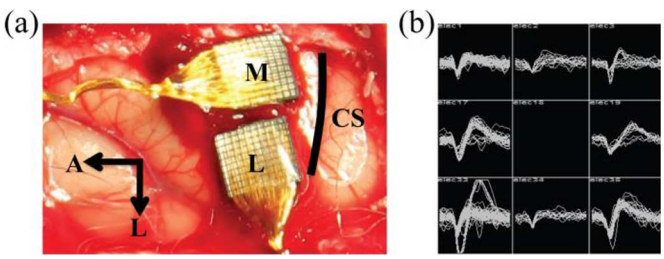

Fig. 3. (a) Surgical photo of two Utah arrays implanted in motor cortex of a rhesus macaque, medial ('M') and lateral ('L') arrays. (b) Representative spike panel from the lateral array, showing well isolated single units.

it was digitized at 30 ks/s by a Cerebus neural signal processor (NSP, Blackrock Microsystems).

A second monkey was implanted with two 96-channel intracortical Utah arrays in primary motor cortex, shown in Fig. 3, by two neurosurgeons experienced in this procedure. To locate the hand area of motor cortex, we first identified the genu of the arcuate sulcus within the craniotomy and projected a line posteriorly to central sulcus. The first array was placed on this line, just anterior to central sulcus, and the second was placed directly medial to the first. Broadband data were recorded at 30 ks/s from the lateral array during task performance using the NSP. Neural spikes were detected by high-pass filtering the raw data at 250 Hz and thresholding the resulting signal at -4.5 times the RMS voltage on each channel.

3) High-Bandwidth Decoding: We analyzed datasets from two separate days for each modality. One was used as a feature selection set, to find the optimal decoding features for each modality, and the other was used as the testing set for both the high-bandwidth and low-bandwidth decodes. No feature selection was performed on the testing set, and each decode was trained and tested on the testing set using cross validation.

For the ECoG datasets, we classified either which grasp was performed (P1, fist versus pinch versus rest), or which finger was stimulated (P2, thumb versus index versus little) on each trial. Movement/stimulation onset for each trial was marked by visual inspection of the kinematic data. We used linear discriminant analysis (LDA) to perform the classification and verified performance with leave-one-out cross validation. Our performance metric was percent correct, and we used an equal number of trials for each movement during decoding.

Using the P1 ECoG feature selection dataset, we found grasp-relevant channels by comparing mean gamma (66–114 Hz) power on each channel during separate thumb and little finger flexion movements. We used the five channels with a significant difference between trial types that also corresponded to motor cortex as mapped by clinical microstimulation. To determine the best high-bandwidth feature for decoding, we performed LDA on the same dataset to classify fist versus pinch grasps, using mean gamma power and beta power (10–30 Hz). We found, similar to several other studies [15], [16], that including beta band activity did not significantly increase classification performance. Similarly, with the P2 ECoG feature selection set, we found the two stimulation-relevant channels that also corresponded to sensory cortex and confirmed that beta did not increase performance. Thus, our high-bandwidth decoding feature was simply mean gamma power from 0.5 s before to 1 s after movement/stimulation onset.

All subsequent testing was performed on the testing day's datasets. The P1 testing dataset contained 51 total trials. The P2 testing set contained 20 trials. The signal-to-noise ratio (SNR) of these datasets was taken as the ratio of mean gamma activity amplitude surrounding movement onset to that during rest periods. For P1 and P2, the mean SNR of all channels was 1.2 and 1.1, respectively.

For the EMG datasets, we predicted finger flexion onset and offset during a contiguous set of movement trials. The testing dataset contained 95 trials (756 time bins). The SNR was taken as the ratio of mean EMG amplitude during finger flexion to that during extension and rest, resulting in an SNR of 5.8 for the testing set. True movement onset and offset times were marked via visual inspection of the kinematic data prior to decoding. Each trial was split into consecutive 64 ms time bins, and we used LDA (with ten-fold cross validation) to predict whether the monkey was flexing or not during each bin. The performance metric was again percent correct, where decode points were marked as correct if onset or offset was correctly detected within 150 ms and the decode remained constant until the next onset or offset. For the high-bandwidth decode, we first filtered the broadband EMG between 100–500 Hz. We then extracted four temporal features of the EMG waveform [20], [35] at each time bin: 1) average absolute signal amplitude; 2) number of zero crossings; 3) number of slope changes; and 4) waveform line length.

For the intracortical datasets, we used a linear Wiener filter [36] to predict the monkey's continuous finger position. The testing dataset contained 152 trials (1535 time bins). The intracortical SNR was taken as the peak-to-peak amplitude of the largest single unit on each channel to twice the standard deviation of the broadband signal on that channel with isolated spikes removed. The mean SNR of all included channels in the testing set was 6.5. We first binned the neural and kinematic data at 64 ms intervals and took ten lagged bins of neural data history for each channel. We then performed least squares linear regression

TABLE II
DECODING FEATURES

Modality	High-Bandwidth Feature	System Configuration	Data Rate	Low-Bandwidth Feature	System Configuration	Data Rate
ECoG	Gamma power	< 1 kHz, 2 ksps	512 kbps	Optimal band power	75-150 Hz, 500 sps	4 kbps*
EMG	Temporal features	100-500 Hz, 5 ksps	1.28 Mbps	Optimal band power	200-500 Hz, 1 ksps	4 kbps*
Intracortical	Spike counts	< 7.5 kHz, 20 ksps	3.84 Mbps**	Optimal band power	300-1000 Hz, 2 ksps	4 kbps*

* Transmitting a single 16-bit average per channel every 64 ms
** 12 bit ADC resolution

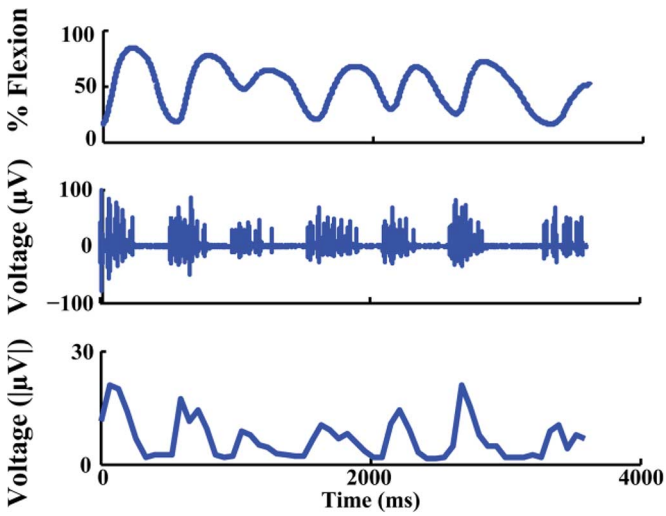

Fig. 4. Real-time MINI recording of *in vivo* EMG during task performance. Top trace: monkey finger position (100 = fully flexed, 0 = fully extended). Middle trace: Broadband EMG recorded simultaneously. Bottom trace: MINI output received every 64 ms, representing mean signal power in 100–500 Hz.

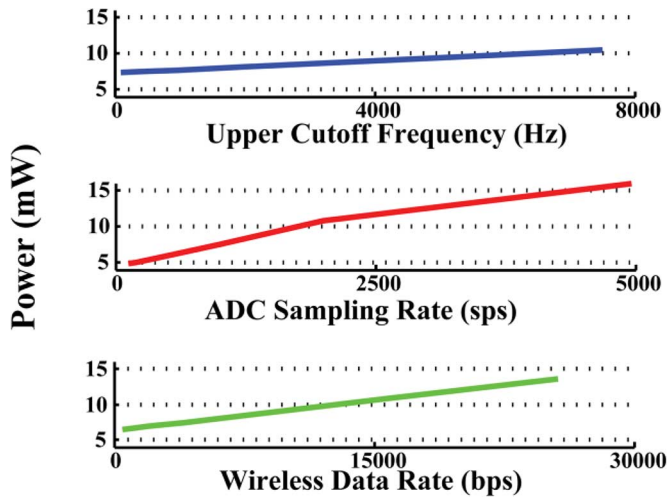

Fig. 5. MINI parameter sweeps showing the individual contribution of each configuration setting to the overall power consumption. The slope of a linear fit to each parameter is 0.43 mW/kHz, 2.31 mW/ks/s, and 0.29 mW/kb/s, respectively, from top to bottom.

to calculate the filter coefficients [36]. We performed ten-fold cross validation for testing and used the correlation coefficient and root-mean-square error as the performance metrics. Using the feature selection day's dataset, we first determined the optimal set of 16 channels (currently, the maximum capability of the MINI) for decoding by performing backward elimination from the full set of 96 channels [37]. This type of neuron selection has been shown previously to improve decoding performance [38]. For the high-bandwidth decode, we used binned spike counts on each of the 16 channels. The high-bandwidth feature for each modality is listed in Table II.

4) Low-Bandwidth Decoding: In MATLAB, using the feature selection datasets, we first found the best individual frequency band for decoding each modality by performing a grid search on the possible upper and lower cutoff frequencies. Using each pair of filter cutoffs, we filtered the broadband data and used the mean signal power on each channel as the decoding feature (using the same methods as the high-bandwidth decode). After finding the optimal bands, we performed the same decodes again with a range of sampling rates to determine the effect, if any, of sampling over or under the Nyquist rate for each band.

Using each modality's testing dataset, we configured the MINI to use the optimal frequency band and sampling rate for that modality and replayed the broadband neural data through the MINI using a National Instruments DAC. The DAC output was adjusted via a voltage divider to achieve the original signal amplitude. The MINI output was recorded by a remote wireless receiver and resynchronized with the kinematics from the same dataset. Finally, the low-bandwidth decode was performed on this new dataset, using the same algorithm and cross-validation process as the high-bandwidth decode for each modality.

5) Power Comparison: In order to compare the power requirements of implantable systems designed for low-bandwidth versus high-bandwidth features, we estimated the power consumption of a system with a similar architecture to the MINI, but designed to transmit full broadband data for each modality. As the MINI was designed for low data rates, we estimated the full broadband power assuming an RF transceiver from the same family, the Atmel AT86RF233, with a maximum throughput of 2 Mb/s. We kept the assumed system specifications as close as possible to the MINI. Power was calculated based on numbers and equations drawn from each component's datasheet and depended primarily on the assumed analog filter cutoff, sampling rate, and wireless data rate. Details of the calculation are given in the Appendix.

III. RESULTS

A. System Validation

To validate the real-time performance of the MINI, we recorded *in vivo* EMG during task performance, while simultaneously recording the full broadband signal with the NSP. The MINI was powered by a single 3.7 V battery and was configured to filter between 100–500 Hz, sample at 1 ks/s, and transmit every 64 ms (250 b/s for a single channel). The

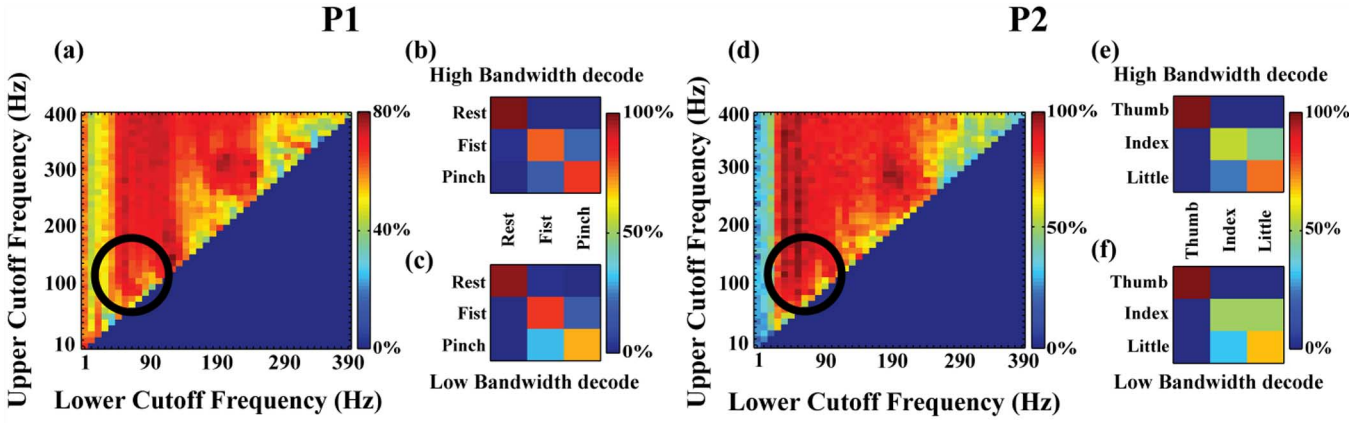

Fig. 6. (a), (d) ECoG decoding performance for P1 and P2, respectively, as a function of the front-end pass-band (black circles mark the optimal pass-band). (b), (e) High-bandwidth decode performance as a confusion matrix for P1 and P2 using gamma power (<1 kHz, 2 ks/s)—percent correct (PC) = 86.4% for P1, PC = 77.3% for P2. (c), (f) Low-bandwidth decode performance for P1 and P2 using the MINI (75–150 Hz, 0.5 ks/s)—PC = 83.3% for P1, PC = 72.7% for P2.

output of the MINI was wirelessly transmitted to a receiver located ∼1 m away, which then sent the received data to the xPC for storage and task synchronization. The MINI output and associated broadband signal are shown in Fig. 4.

We also explored the contribution of each configurable parameter to system power consumption by performing a sweep of the parameter space (amplifier upper cutoff frequency, per-channel sampling rate, and total wireless data rate). During each single parameter sweep, the remaining parameters were held constant at a cutoff of 500 Hz, a sampling rate of 1 ks/s, and a wireless bit rate of 4 kb/s (transmitting 16 channels of 16-bit data every 64 ms). The individual sweeps are shown in Fig. 5. A linear fit to each curve yields a slope of 0.43 mW/kHz, 2.31 mW/ks/s, and 0.29 mW/kb/s, respectively.

As each slope is positive, the optimal setting for each parameter is the minimum value which does not significantly decrease decoding ability. In particular, sampling rate appears to be the main driver of power consumption in this system. However, it is primarily limited by the analog upper cutoff frequency, such that we can potentially reduce power consumption by minimizing the cutoff frequency and sampling at the Nyquist rate. Further, the wireless data rate is required to be fast enough that a clinical BMI could respond to neural commands with no noticeable lag, limiting the power optimization of this setting. Thus, the primary target of MINI optimization discussed here is upper cutoff frequency.

B. Modality I—ECoG

We used ECoG data to classify either which grasp (fist, pinch, or rest) a human subject (P1) performed on a given trial, or which finger (thumb, index, or little) of a second subject (P2) was stimulated. In order to find the optimal MINI filter cutoffs for decoding ECoG data, we performed these classifications in MATLAB using various pass-bands. Decode performance for each subject as a function of the lower and upper cutoff frequency is shown as a heatmap in Fig. 6(a), (d). Only performance values above the diagonal are shown, as by definition the upper cutoff is larger than the lower cutoff. As the sampling rate was shown in Fig. 5 to be the main driver of power consumption, the optimal MINI configuration should minimize the upper cutoff frequency, allowing the required Nyquist sampling rate to decrease. Thus, the optimal setting can be found from the heatmaps in Fig. 6 as the cluster of high performance values nearest the lower left corner, ∼60–120 Hz [black circles in Fig. 6(a) and (d)]. This identified optimal band did not change considerably when Gaussian white noise was added to the signal prior to decoding in MATLAB.

Using this pass-band, we repeated the classification for P1 using a range of sampling rates and found considerable performance decreases when sampling below 500 sps. To provide a decodable output at BMI-relevant timescales, we set the bin period to 64 ms. At 16 channels and 16-bit resolution, this results in a wireless data rate of 4 kb/s. These settings are summarized in Table II, along with those for the EMG and intracortical modalities.

Using these optimal parameters, we ran the neural data from the testing datasets through the MINI and recorded the output. In this configuration, the MINI consumed 5.9 mW of power. To estimate the power consumption of a system similar to the MINI, but designed to extract the high-bandwidth ECoG feature (gamma power extracted from the broadband data), we assumed an upper cutoff frequency of 1 kHz and a 2 ks/s sampling rate. This configuration, listed in Table II, would allow for the extraction of all commonly used ECoG frequency bands [15]. At 16-bit resolution, transmitting 16 channels of broadband would result in a wireless data rate of 512 kb/s. The estimated power for this system, using the datasheet from a high-bandwidth Atmel wireless transceiver from the same family as the MINI transceiver, was 15.8 mW. In this case, the MINI reduced the necessary power by 62.7% of the high-bandwidth consumption.

We decoded the MINI output, as shown in Fig. 6(c) and (f), yielding a percent correct (PC) of 83.3% for P1 and 72.7% for P2. We decoded these same datasets in MATLAB using the high-bandwidth ECoG feature, yielding PC = 86.4% for P1 and PC = 77.3% for P2, as shown in Fig. 6(b) and (e). Thus for a power reduction of 62.7%, the low-bandwidth MINI decodes represent losses of only 3.6% and 6.0% of the high-bandwidth performance for P1 and P2, respectively. These results are summarized in Table III for each modality.

TABLE III
SUMMARY OF DECODING PERFORMANCE AND POWER CONSUMPTION

Modality	Full decoding performance [95% CI]	MINI decoding performance [95% CI]	Percent change from full decode	Full power consumption	MINI power consumption	Percent change from full power
ECoG (P1)	PC = 86.4% [70.8, 95.5]	PC = 83.3% [67.2, 93.6]	-3.6%	15.8 mW	5.9 mW	-62.7%
ECoG (P2)	PC = 77.3% [49.0, 94.4]	PC = 72.7% [44.2, 91.8]	-6.0%	15.8 mW	5.9 mW	-62.7%
EMG	PC = 95.3% [93.6, 96.8]	PC = 92.6% [90.2, 94.1]	-2.8%	35.3 mW	7.5 mW	-78.8%
Intracortical	ρ = 0.82 [0.81, 0.84], RMSE = 0.172	ρ = 0.78 [0.77, 0.80], RMSE = 0.186	-4.9%, +8.1%	105.9 mW	10.9 mW	-89.7%

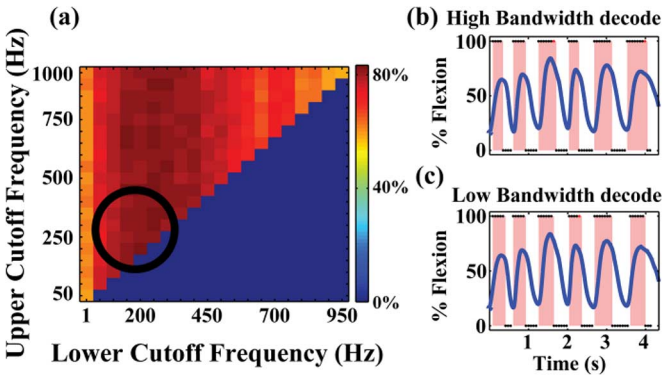

Fig. 7. (a) EMG decoding performance as a function of the front-end pass-band (black circle marks the optimal pass-band). (b) High-bandwidth decode using temporal waveform features, pink indicates predicted flexion (200–500 Hz, 5 ks/s)—percent correct = 95.3%. (c) Low-bandwidth decoding performance using the MINI (200–500 Hz, 1 ks/s)—percent correct = 92.6%.

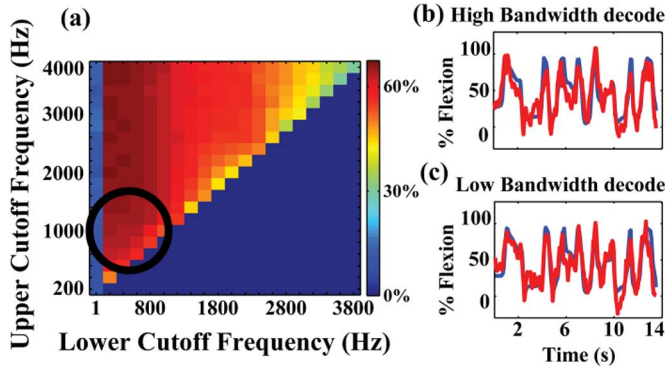

Fig. 8. (a) Intracortical decoding performance as a function of the front-end pass-band (black circle marks the optimal pass-band). (b) High-bandwidth decode using spike counts, blue trace is the actual finger position, red is the predicted position (<7.5 kHz, 20 ks/s)—correlation (ρ) = 0.82 and root-mean-square error (RMSE) = 0.172. (c) Low-bandwidth decoding performance using the MINI (0.3–1 kHz, 2 ks/s)—ρ = 0.78 and RMSE = 0.186.

C. Modality II—EMG

We used EMG data to predict whether or not a monkey was flexing his fingers at a given time point. To find the optimal MINI filter cutoffs for decoding EMG, we performed this decode in MATLAB using various pass-bands. Decode performance is shown in Fig. 7(a) as a function of the cutoff frequencies. The optimal pass-band was found to be ~200–400 Hz, and was robust to simulated signal white noise. Due to a limited number of filter configuration values on the Intan amplifier, we used a pass-band of 200–500 Hz to best represent this optimal band. Using this band with a range of sampling rates, the optimal setting was the Nyquist rate of 1 ks/s. We also used the same wireless data rate as ECoG, transmitting 16 channels every 64 ms (4 kb/s).

In this configuration, when processing a separate testing dataset, the MINI consumed 7.5 mW of power. To estimate the high-bandwidth system power, we assumed a pass-band of 100–500 Hz and sampling rate of 5 ks/s to enable extraction of temporal waveform features. Transmitting 16 channels at 16-bit resolution requires a wireless data rate of 1.28 Mb/s. The estimated power for this system was 35.3 mW, indicating that the MINI reduced the necessary power by 78.8%.

Decoding the MINI output resulted in a PC = 92.6%, shown in Fig. 7(c). Decoding the same dataset in MATLAB using the high-bandwidth EMG feature set yielded PC = 95.3%, as shown in Fig. 7(b). Thus for a power reduction of 78.8%, the low-bandwidth MINI decode loses only 2.8% of the high-bandwidth performance.

D. Modality III—Intracortical

Finally, we used intracortical data to predict a monkey's continuous finger position via a linear Wiener filter [36]. To find the optimal MINI filter settings for decoding intracortical data, we repeated this decode in MATLAB using various pass-bands. Decode performance (correlation coefficient) is shown in Fig. 8(a) as a function of the cutoff frequencies. The optimal pass-band was found to be ~300–1000 Hz, and the optimal sampling rate to be the Nyquist rate of 2 ks/s. This is consistent with a view that most of the information in intracortical data can be found in spikes with a ~1 ms sinusoidal waveform. This pass-band sacrifices some potential performance in order to reduce the required sampling rate, and therefore save power. It did not change considerably with simulated white noise conditions. We used the same wireless data rate as previously, 4 kb/s when transmitting every 64 ms.

In this configuration, when processing the testing dataset, the MINI consumed 10.9 mW of power. To estimate the power consumed by a high-bandwidth system designed to extract neural spikes, we assumed a pass-band of .1–7500 Hz and a sampling rate of 20 ks/s, similar to existing systems [10]. The resulting data rate for this configuration was 3.84 Mb/s when using 12-bit resolution. As this data rate was beyond the 2 Mb/s maximum of the assumed transceiver, we further assumed the system to have two identical transceivers, each transmitting the data from eight channels (a per-chip data rate of 1.92 Mb/s). The estimated power for this system was 105.9 mW, indicating that the MINI reduced the necessary power by 89.7%.

TABLE IV
COMPARISON OF MINI TO INTRACORTICAL ASIC-BASED SYSTEMS

Reference	No. channels	Upper cutoff frequency	Sampling rate per channel	Total data rate	Amplifier input-referred noise	Total power consumption	Power per channel
Chae, 2009 [11]	128	10 kHz	40 kSps	90 Mbps	4.9 μV_{rms}	6 mW	46.8 μW
Gosselin, 2009 [28]	16	9.2 kHz	30 kSps	< 1 Mbps	5.4 μV_{rms}	2.21 mW	138 μW
Wattanapanitch, 2011 [40]	32	12 kHz	31.25 kSps	8 Mbps	5.4 μV_{rms}	325 μW	10.2 μW
Borton, 2013 [10]	100	7.8 kHz	20 kSps	24 Mbps	8.6 μV_{rms}	90.6 mW	906 μW
Yin, 2013 [9]	100	7.8 kHz	20 kSps	24 Mbps	2.83 μV_{rms}	51 mW	510 μW
This work	**16**	**1 kHz**	**2 kSps**	**4 kbps**	**2.4 μV_{rms}**	**10.9 mW**	**681 μW**

Decoding the low-bandwidth MINI output resulted in a correlation coefficient (ρ) of 0.78 between actual and predicted finger position, and root mean squared error (RMSE) of 0.186, as shown in Fig. 8(c). Using the high-bandwidth feature, spike counts detected in the broadband by thresholding, we decoded the same dataset with $\rho = 0.82$ and RMSE $= 0.172$, as shown in Fig. 8(b). Thus for a power reduction of 89.7%, the low-bandwidth MINI decode loses only 4.9% of the high-bandwidth correlation coefficient and increases the high-bandwidth RMSE by only 8.1%.

IV. DISCUSSION

We have demonstrated that signal power within a narrow frequency band, sampled below 2 ks/s, can be used to accurately decode information from multiple, disparate neural sources. We designed and built a miniature neural recording system to extract this feature and verified that decoding performance was similar to using high-bandwidth, modality-specific features. Performance decreased by less than 9% when decoding continuous finger movement from intracortical data or when classifying the target of sensory stimulation from ECoG data, less than 5% when classifying grasp type from ECoG data or when predicting finger flexion from EMG recordings. Further, the decode performances and identified optimal frequency bands were robust to added signal noise. Decoding performance was similar to that reported by other groups using modality-specific features [16], [39].

In contrast, the power consumption saved when extracting our low-bandwidth feature on-chip relative to a system designed to transmit the full broadband signal varied from 62.8% for ECoG to 89.7% for intracortical. This dramatic decrease in power enables not only longer-lasting devices, but also higher channel counts which should more than offset the slightly lower decoding performance. Our system was designed to transmit 16 channels of neural data. Assuming linear scaling of power consumption, our system would require only 68.1 mW to transmit 100 channels of intracortical data, ten times less than the 661.9 mW for a broadband design.

It could be argued that low-power ASIC-based systems are capable of enabling viable broadband designs without our approach. Chae *et al.*, for example, designed a 128 channel intracortical system which draws only 6 mW to transmit broadband data below 20 kHz (sampled at 40 ks/s) [11]. Wattanapanitch and Sarpeshkar similarly designed a neural recording IC which digitized 32 channels of intracortical broadband for only 325 μW (a per-channel cost of only 10.2 μW) [40]. A comparison of these and several other ASIC-based systems to the MINI is presented in Table IV, clearly showing that an ASIC can achieve much lower power than an off-the-shelf solution such as the MINI.

However, these approaches are not mutually exclusive. If power reductions similar to those shown here for the MINI could be applied to the already low-power designs of [11] and [40], for example, this would result in a *total* cost of only 618 μW and 33.5 μW, respectively. This puts such systems much closer to being able to operate for long periods on a battery, without inductive charging or with only rare recharges necessary, which would ease the transition into the clinical setting. If higher power consumption is still acceptable, the power savings can be used to increase channel counts and gather information from many more neural sources.

Additionally, producing high-bandwidth data requires excessive hardware on the receiving end, in order to extract the necessary decoding features (a low-bandwidth signal in any case). Systems designed to record and decode neural data entirely inside the body (e.g., functional electrical stimulation [41]) would be required us to either also implant fast, power-hungry processors in order to deal with the added data load, further reducing battery life, or require the patient to use an unnecessary external processor.

Our system demonstrates that accurate, clinically useful information can be extracted from a feature space shared by the three most commonly used neural modalities, which also allows for a substantial reduction in power consumption. We believe that this represents a viable commercial device architecture by enabling long-lasting and high channel-count implantable systems for use in multiple clinical markets.

APPENDIX

Broadband system power was estimated based on a system similar to the MINI, using an Intan RHD2216 amplifier, Atmel ATMega328p MCU, and an Atmel AT86RF233 wireless transceiver. In a simplified model of the system, the amplifier draws a constant current after being configured, the MCU draws a large current when actively retrieving data from the amplifier and is in low-power mode for the rest of the sampling period, and the transceiver draws a large current when actively transmitting and is in low-power mode otherwise.

The amplifier current draw depends only on the configured filter upper cutoff frequency, f_c, and the per-channel sampling rate, f_s. With all 16 channels active, the current is

$$I_{\text{amp}} = 710\ \mu A + 121.6\frac{\mu A}{\text{kHz}} * f_c + 34.24\frac{\mu A}{\text{ks/s}} * f_s. \quad (1)$$

The MCU current draw depends both on the MCU clock rate, f_{mcu}, and on f_s to determine the active duty cycle. For the ECoG and EMG modalities, we assumed a clock of 8 MHz in order to achieve the same SPI clock rate (half the MCU clock) as the MINI. For this clock rate, the large active current, I_a, is 3 mA and the low-power mode current, I_s, is 1 μA. The higher sampling rate of intracortical data required the assumption of a higher MCU clock of 12 MHz, increasing I_a to 4 mA. For 16 channels of 16-bit data, MCU current is

$$I_{\mathrm{mcu}} = I_a * \frac{512 * f_s}{f_{\mathrm{mcu}}} + I_s * \left(1 - \frac{512 * f_s}{f_{\mathrm{mcu}}}\right). \quad (2)$$

Wireless current assumed it was transmitting at maximum power at 2 Mb/s. When actively transmitting, it draws 13.8 mA and draws 0.4 μA for the rest of the sampling period. The time spent in each mode depends on the total amount of data transmitted, N_{bits}. For ECoG and EMG, N_{bits} was 256 bits at 16-bit resolution. For intracortical, the high sampling rate required a further assumption that the system have two identical RF transceivers, each transmitting the data from eight channels at 12-bit resolution. Thus, N_{bits} for intracortical was 96 bits, and the total wireless current draw was doubled

$$I_{rf} = 13.8\ \mathrm{mA} * \frac{N_{\mathrm{bits}} * f_s}{2\ \mathrm{Mb/s}} + 0.4\ \mu A * \left(1 - \frac{N_{\mathrm{bits}} * f_s}{2\ \mathrm{Mb/s}}\right). \quad (3)$$

The total broadband system power was then the sum of all component currents multiplied by the supply voltage

$$P = (I_{\mathrm{amp}} + I_{\mathrm{mcu}} + I_{rf}) * 3.3\ V. \quad (4)$$

REFERENCES

[1] M. Velliste, S. Perel, M. C. Spalding, A. S. Whitford, and A. B. Schwartz, "Cortical control of a prosthetic arm for self-feeding," *Nature*, vol. 453, no. 7198, pp. 1098–1101, May 2008.

[2] V. Gilja, P. Nuyujukian, C. A. Chestek, J. P. Cunningham, B. M. Yu, J. M. Fan, M. M. Churchland, M. T. Kaufman, J. C. Kao, S. I. Ryu, and K. V. Shenoy, "A high-performance neural prosthesis enabled by control algorithm design," *Nat. Neurosci.*, vol. 15, no. 12, pp. 1752–1757, Dec. 2012.

[3] C. Ethier, E. R. Oby, M. J. Bauman, and L. E. Miller, "Restoration of grasp following paralysis through brain-controlled stimulation of muscles," *Nature*, vol. 485, no. 7398, pp. 368–371, May 2012.

[4] J. L. Collinger, B. Wodlinger, J. E. Downey, W. Wang, E. C. Tyler-Kabara, D. J. Weber, A. J. C. McMorland, M. Velliste, M. L. Boninger, and A. B. Schwartz, "High-performance neuroprosthetic control by an individual with tetraplegia," *Lancet*, vol. 381, no. 9866, pp. 557–564, Feb. 2013.

[5] L. R. Hochberg, D. Bacher, B. Jarosiewicz, N. Y. Masse, J. D. Simeral, J. Vogel, S. Haddadin, J. Liu, S. S. Cash, P. van der Smagt, and J. P. Donoghue, "Reach and grasp by people with tetraplegia using a neurally controlled robotic arm," *Nature*, vol. 485, no. 7398, pp. 372–375, May 2012.

[6] M. Rizk, C. A. Bossetti, T. A. Jochum, S. H. Callender, M. A. L. Nicolelis, D. A. Turner, and P. D. Wolf, "A fully implantable 96-channel neural data acquisition system," *J. Neural Eng.*, vol. 6, no. 2, p. 026002, Apr. 2009.

[7] W. R. Patterson, Y.-K. Song, C. W. Bull, I. Ozden, A. P. Deangellis, C. Lay, J. L. McKay, A. V. Nurmikko, J. D. Donoghue, and B. W. Connors, "A microelectrode/microelectronic hybrid device for brain implantable neuroprosthesis applications," *IEEE Trans. Biomed. Eng.*, vol. 51, no. 10, pp. 1845–1853, Oct. 2004.

[8] T. A. Szuts, V. Fadeyev, S. Kachiguine, A. Sher, M. V. Grivich, M. Agrochão, P. Hottowy, W. Dabrowski, E. V. Lubenov, A. G. Siapas, N. Uchida, A. M. Litke, and M. Meister, "A wireless multi-channel neural amplifier for freely moving animals," *Nat. Neurosci.*, vol. 14, no. 2, pp. 263–269, Feb. 2011.

[9] M. Yin, H. Li, C. Bull, D. A. Borton, J. Aceros, L. Larson, and A. V. Nurmikko, "An externally head-mounted wireless neural recording device for laboratory animal research and possible human clinical use," in *Proc. 35th Annu. Int. Conf. IEEE Engineering in Medicine Biology Soc. (EMBS)*, 2013, pp. 3109–3114.

[10] D. A. Borton, M. Yin, J. Aceros, and A. Nurmikko, "An implantable wireless neural interface for recording cortical circuit dynamics in moving primates," *J. Neural Eng.*, vol. 10, no. 2, p. 026010, Apr. 2013.

[11] M.-S. Chae, Z. Yang, M. R. Yuce, L. Hoang, and W. Liu, "A 128-channel 6 mW wireless neural recording IC with spike feature extraction and UWB transmitter," *IEEE Trans. Neural Syst. Rehabil. Eng.*, vol. 17, no. 4, pp. 312–321, Aug. 2009.

[12] Code of Federal Regulations (CFR) Title 47, Telecommunication, Part 95.663(d) Emission Bandwidth, [Online] Available: [Online]. Available: http://www.ecfr.gov/cgi-bin/text-idx?tpl=/ecfrbrowse/Title47/47cfr95_main_02.tpl

[13] V. S. Mallela, V. Ilankumaran, and N. S. Rao, "Trends in cardiac pacemaker batteries," *Indian Pacing Electrophysiol. J.*, vol. 4, no. 4, pp. 201–212, Oct. 2004.

[14] H. Miranda, V. Gilja, C. A. Chestek, K. V. Shenoy, and T. H. Meng, "HermesD: A high-rate long-range wireless transmission system for simultaneous multichannel neural recording applications," *IEEE Trans. Biomed. Circuits Syst.*, vol. 4, no. 3, pp. 181–191, Jun. 2010.

[15] T. Pistohl, A. Schulze-Bonhage, A. Aertsen, C. Mehring, and T. Ball, "Decoding natural grasp types from human ECoG," *NeuroImage*, vol. 59, no. 1, pp. 248–260, Jan. 2012.

[16] C. A. Chestek, V. Gilja, C. H. Blabe, B. L. Foster, K. V. Shenoy, J. Parvizi, and J. M. Henderson, "Hand posture classification using electrocorticography signals in the gamma band over human sensorimotor brain areas," *J. Neural Eng.*, vol. 10, no. 2, p. 026002, Apr. 2013.

[17] F. Zhang, A. Mishra, A. Richardson, and B. Otis, "A low-power ECoG/EEG processing IC with integrated multiband energy extractor," *IEEE Trans. Circuits Syst.*, vol. 58, no. 9, pp. 2069–2082, Sep. 2011.

[18] D. Farina, N. Jiang, H. Rehbaum, A. Holobar, B. Graimann, H. Dietl, and O. C. Aszmann, "The extraction of neural information from the surface EMG for the control of upper-limb prostheses: Emerging avenues and challenges," *IEEE Trans. Neural Syst. Rehabil. Eng.*, vol. 22, no. 4, pp. 797–809, Jul. 2014.

[19] R. L. Hart, N. Bhadra, F. W. Montague, K. L. Kilgore, and P. H. Peckham, "Design and testing of an advanced implantable neuroprosthesis with myoelectric control," *IEEE Trans. Neural Syst. Rehabil. Eng.*, vol. 19, no. 1, pp. 45–53, Feb. 2011.

[20] P. Zhou, M. M. Lowery, K. B. Englehart, H. Huang, G. Li, L. Hargrove, J. P. A. Dewald, and T. A. Kuiken, "Decoding a new neural machine interface for control of artificial limbs," *J. Neurophysiol.*, vol. 98, no. 5, pp. 2974–2982, Sep. 2007.

[21] R. F. Weir, P. R. Troyk, G. A. DeMichele, D. A. Kerns, J. F. Schorsch, and H. Maas, "Implantable myoelectric sensors (IMESs) for intramuscular electromyogram recording," *IEEE Trans. Biomed. Eng.*, vol. 56, no. 1, pp. 159–171, Jan. 2009.

[22] B. D. Farnsworth, D. M. Talyor, R. J. Triolo, and D. J. Young, "Wireless in vivo EMG sensor for intelligent prosthetic control," in *Proc. Int. Conf. Solid-State Sensors, Actuators and Microsystems TRANSDUCERS*, 2009, pp. 358–361.

[23] M. D. Serruya, N. G. Hatsopoulos, L. Paninski, M. R. Fellows, and J. P. Donoghue, "Brain-machine interface: Instant neural control of a movement signal," *Nature*, vol. 416, no. 6877, pp. 141–142, Mar. 2002.

[24] L. R. Hochberg, M. D. Serruya, G. M. Friehs, J. A. Mukand, M. Saleh, A. H. Caplan, A. Branner, D. Chen, R. D. Penn, and J. P. Donoghue, "Neuronal ensemble control of prosthetic devices by a human with tetraplegia," *Nature*, vol. 442, no. 7099, pp. 164–171, Jul. 2006.

[25] G. Santhanam, S. I. Ryu, B. M. Yu, A. Afshar, and K. V. Shenoy, "A high-performance brain-computer interface," *Nature*, vol. 442, no. 7099, pp. 195–198, Jul. 2006.

[26] R. H. Olsson and K. D. Wise, "A three-dimensional neural recording microsystem with implantable data compression circuitry," *IEEE J. Solid-State Circuits*, vol. 40, no. 12, pp. 2796–2804, Dec. 2005.
[27] A. Sodagar, G. E. Perlin, Y. Yao, K. Najafi, and K. D. Wise, "An implantable 64-channel wireless microsystem for single-unit neural recording," *IEEE J. Solid-State Circuits*, vol. 44, no. 9, pp. 2591–2604, Sep. 2009.
[28] B. Gosselin, A. Ayoub, J.-F. Roy, M. Sawan, F. Lepore, A. Chaudhuri, and D. Guitton, "A mixed-signal multichip neural recording interface with bandwidth reduction," *IEEE Trans. Biomed. Circuits Syst.*, vol. 3, no. 3, pp. 129–141, Jun. 2009.
[29] C. A. Chestek, V. Gilja, P. Nuyujukian, R. J. Kier, F. Solzbacher, S. I. Ryu, R. R. Harrison, and K. V. Shenoy, "HermesC: Low-power wireless neural recording system for freely moving primates," *IEEE Trans. Neural Syst. Rehabil. Eng.*, vol. 17, no. 4, pp. 330–338, Aug. 2009.
[30] R. R. Harrison, R. J. Kier, C. A. Chestek, V. Gilja, P. Nuyujukian, S. Ryu, B. Greger, F. Solzbacher, and K. V. Shenoy, "Wireless neural recording with single low-power integrated circuit," *IEEE Trans. Neural Syst. Rehabil. Eng.*, vol. 17, no. 4, pp. 322–329, Aug. 2009.
[31] D. Cheney, A. Goh, J. Xu, K. Gugel, J. G. Harris, J. C. Sanchez, and J. C. Principe, "Wireless, in vivo neural recording using a custom integrated bioamplifier and the pico system," in *Proc. 3rd Int. IEEE/EMBS Conf. Neural Engineering CNE'07*, 2007, pp. 19–22.
[32] E. Stark and M. Abeles, "Predicting movement from multiunit activity," *J. Neurosci.*, vol. 27, no. 31, pp. 8387–8394, Aug. 2007.
[33] M. G. Dorman, M. Prisbe, and J. D. Meindl, "A monolithic signal processor for a neurophysiological telemetry system," *IEEE J. Solid-State Circuits*, vol. 20, no. 6, pp. 1185–1193, Dec. 1985.
[34] K. A. Ludwig, R. M. Miriani, N. B. Langhals, M. D. Joseph, D. J. Anderson, and D. R. Kipke, "Using a common average reference to improve cortical neuron recordings from microelectrode arrays," *J. Neurophysiol.*, vol. 101, no. 3, pp. 1679–1689, Mar. 2009.
[35] B. Hudgins, P. Parker, and R. N. Scott, "A new strategy for multifunction myoelectric control," *IEEE Trans. Biomed. Eng.*, vol. 40, no. 1, pp. 82–94, Jan. 1993.
[36] C. A. Chestek, V. Gilja, P. Nuyujukian, J. D. Foster, J. M. Fan, M. T. Kaufman, M. M. Churchland, Z. Rivera-Alvidrez, J. P. Cunningham, S. I. Ryu, and K. V. Shenoy, "Long-term stability of neural prosthetic control signals from silicon cortical arrays in rhesus macaque motor cortex," *J. Neural Eng.*, vol. 8, no. 4, p. 045005, Aug. 2011.
[37] H. Cecotti, B. Rivet, M. Congedo, C. Jutten, O. Bertrand, E. Maby, and J. Mattout, "A robust sensor-selection method for P300 brain-computer interfaces," *J. Neural Eng.*, vol. 8, no. 1, p. 016001, Feb. 2011.
[38] R. Wahnoun, J. He, and S. I. H. Tillery, "Selection and parameterization of cortical neurons for neuroprosthetic control," *J. Neural Eng.*, vol. 3, no. 2, p. 162, Jun. 2006.
[39] V. Aggarwal, M. Mollazadeh, A. G. Davidson, M. H. Schieber, and N. V. Thakor, "State-based decoding of hand and finger kinematics using neuronal ensemble and LFP activity during dexterous reach-to-grasp movements," *J. Neurophysiol.*, vol. 109, no. 12, pp. 3067–3081, Jun. 2013.
[40] W. Wattanapanitch and R. Sarpeshkar, "A low-power 32-channel digitally programmable neural recording integrated circuit," *IEEE Trans. Biomed. Circuits Syst.*, vol. 5, no. 6, pp. 592–602, Dec. 2011.
[41] J. Hobby, P. N. Taylor, and J. Esnouf, "Restoration of tetraplegic hand function by use of the neurocontrol freehand system," *J. Hand Surg. Br. Eur.*, vol. 26, no. 5, pp. 459–464, Oct. 2001.

Zachary T. Irwin (S'14) received the B.S. degree in electrical engineering from the Georgia Institute of Technology, Atlanta, GA, USA, the M.S.E. degree in biomedical engineering from the University of Michigan, Ann Arbor, MI, USA, and is currently working toward the Ph.D. degree in biomedical engineering at the University of Michigan.

His research focuses on the extraction of neuroprosthetic control signals for the purpose of dexterous finger and hand movements.

David E. Thompson (M'06) was born in Emporia, KS, USA. He received the B.S. degree in electrical engineering from Kansas State University, USA, in 2006, the M.S. degree in electrical engineering, and both M.S. and Ph.D. degrees in biomedical engineering from the University of Michigan, Ann Arbor, USA, in 2012.

From 2012 to 2013, he was a Post-Doctoral Research Fellow at the University of Michigan. In 2013, he became an Assistant Professor of electrical and computer engineering at Kansas State University, Manhattan, KS. He is the author of ten full-length scientific articles. His research interests include brain-computer interfaces, performance measurement, and non-invasive sensing.

Karen E. Schroeder received the B.S. degree in biomedical engineering from Duke University, Durham, NC, USA, in 2010. She is currently working toward the Ph.D. degree in biomedical engineering at the University of Michigan, Ann Arbor, MI, USA.

Her research is focused on neuroprosthetics and cortical functional connectivity of single neurons and ensembles.

Derek M. Tat, photograph and biography not available at the time of publication.

Ali Hassani was born in Ann Arbor, MI, USA, in 1992. He received the bachelor degrees in biomedical engineering, electrical engineering, and mathematics from the University of Michigan, Ann Arbor, USA, in 2014.

From 2010 to 2014, he was an undergraduate Research Assistant at various Michigan biomedical engineering labs. Since graduating, he has been a Research Engineer at Ford Motor Company. His interests include biomedical control systems, brain machine interface, and neural networks.

Autumn J. Bullard received the B.S. degree in electronics engineering from Norfolk State University, Norfolk, VA, USA, in 2013. She is currently pursuing the Ph.D. degree in biomedical engineering at the University of Michigan, Ann Arbor, MI, USA.

From 2010 to 2012, she was a Summer Research Fellow at West Virginia University, University of Missouri, and Georgia Institute of Technology. Her research interests include the development of low power, fully implantable neuroprosthetic devices to be used for cortically controlled functional electrical stimulation to assist in rehabilitation.

Ms. Bullard is a recipient of the National Science Foundation Fellowship. She is also a member of the Society for Neuroscience as well as the National Society of Black Engineers.

Shoshana L. Woo is currently a plastic and reconstructive surgery resident at the University of Michigan, Ann Arbor, MI, USA. She attended Yale University, New Haven, CT, USA, for her undergraduate studies and Duke University, Durham, NC, USA, for medical school.

Dr. Woo is interested in microsurgery, peripheral nerve surgery, and limb salvage.

Melanie G. Urbanchek (M'13) received the B.S. degree from Ohio University, Athens, OH, USA, the M.S. degree from California State University, Fullerton, CA, USA, and the Ph.D. degree from the University of Southern California, Los Angeles.

She has authored numerous scientific journal articles and has presented her work nationally. Her achievements include developing younger investigators by teaching skills which support a career in clinical medicine with academic research.

Dr. Urbanchek is an active member of several national specialty societies including the American Society of Peripheral Nerve, Plastic Surgery Research Council, the American College for Sports Medicine, and Sigma Xi Scientific Honorary Society.

Adam J. Sachs received the B.Sc. degree at McGill University, Canada, in physiology and math, and M.Sc. degree at York University in applied mathematics researching mechanisms of human edge detection. During his neurosurgery residency at The University of Ottawa, he participated in the Clinical Investigator program, performing neurophysiology and brain computer interface research in non-human primates. After residency, he completed a two-year fellowship in functional neurosurgery at Stanford University, Stanford, CA, USA.

Currently, he is Director of Neuromodulation and Functional Neurosurgery, The Ottawa Hospital, and Assistant Professor of Surgery at The University of Ottawa Brain and Mind Research Institute. His lab investigates potential brain computer interfaces in human basal ganglia and prefrontal cortex.

Paul S. Cederna is the Robert Oneal Professor of Plastic Surgery, Chief of the Section of Plastic Surgery, and Professor in the Department of Biomedical Engineering at the University of Michigan, Ann Arbor, MI, USA. By combining his clinical training in general surgery, microsurgery, and plastic surgery and background in biomedical engineering, he is able to incorporate creative solutions to solve the most difficult clinical problems. He directs the Neuromuscular Research Laboratory at the University of Michigan, has authored over 160 scientific manuscripts, published 20 book chapters, presented his work over 550 times, and has given over 300 extramural presentations.

Dr. Cederna has received 65 national research awards. He has been the Chairman of the Plastic Surgery Research Council, President of the American Society for Peripheral Nerve, is on the Board of Directors of the American Board of Plastic Surgery, and is currently President-Elect of the Plastic Surgery Foundation.

William C. Stacey is an Assistant Professor of neurology and biomedical engineering at the University of Michigan, Ann Arbor, MI, USA. In addition to his duties as an epilepsy physician, Dr. Stacey is developing engineering and mathematical tools to understand seizure dynamics and biomarkers and develop next-generation implantable anti-seizure devices.

Parag G. Patil received the M.D. and Ph.D. degrees from Johns Hopkins University, Baltimore, MD, USA.

He is an Assistant Professor of neurosurgery, neurology, anesthesiology, and biomedical engineering at the University of Michigan, Ann Arbor, MI, USA, which he joined in 2005.

Cynthia A. Chestek (S'04-M'10) was born in Erie, PA, USA. She received the B.S. and M.S. degrees in electrical engineering from Case Western Reserve University, Cleveland, OH, USA, in 2005, and the Ph.D. degree in electrical engineering from Stanford University, Stanford, CA, USA, in 2010.

From 2010 to 2012, she was a Research Associate at the Stanford Department of Neurosurgery. In 2012 she became an Assistant Professor of biomedical engineering at the University of Michigan, Ann Arbor, MI, USA. She is the author of 26 full-length scientific articles. Her research interests include high-density interfaces to the nervous system for the control of multiple degree of freedom hand and finger movements.